

Measurement of Medial Elbow Joint Space using Landmark Detection

Shizuka Akahori^{1*}, Shotaro Teruya², Pragyan Shrestha¹,
Yuichi Yoshii³, Ryuhei Michinobu⁴, Satoshi Iizuka⁵,
Itaru Kitahara⁵

^{1*}Graduate School of Science and Technology, University of Tsukuba,
1-1-1 Tennodai, Tsukuba, 305-8571, Ibaraki, Japan.

^{2*}Department of Orthopaedic Surgery, University of Tsukuba, 1-1-1
Tennodai, Tsukuba, 305-8571, Ibaraki, Japan.

³Department of Orthopaedic Surgery, Ibaraki Medical Center, Tokyo
Medical University, 3-20-1 Ami, Inashiki, 300-0332, Ibaraki, Japan.

^{4*}, Tsukuba Wellness Orthopaedics, 2011-54 Sasagi, Tsukuba, 305-0043 ,
Ibaraki, Japan.

^{5*}Institute of Systems and Information Engineering, University of
Tsukuba, 1-1-1 Tennodai, Tsukuba, 305-8571, Ibaraki, Japan.

*Corresponding author(s). E-mail(s):

akahori.shizuka@image.iit.tsukuba.ac.jp;

Contributing authors: steruya@tsukuba-seikei.jp;

shrestha.pragyan@image.iit.tsukuba.ac.jp; yyoshii@tsukuba-seikei.jp;

michinobu@tsukuba-seikei.jp; iizuka@cs.tsukuba.ac.jp;

kitahara@ccs.tsukuba.ac.jp;

Abstract

Ultrasound imaging of the medial elbow is crucial for the early identification of Ulnar Collateral Ligament (UCL) injuries. Specifically, measuring the elbow joint space in ultrasound images is used to assess the valgus instability of elbow. To automate this measurement, a precisely annotated dataset is necessary; however, no publicly available dataset has been proposed thus far. This study introduces a novel ultrasound medial elbow dataset for measuring joint space to diagnose Ulnar Collateral Ligament (UCL) injuries. The dataset comprises 4,201 medial elbow ultrasound images from 22 subjects, with landmark annotations on the humerus and ulna. The annotations are made precisely by the authors under the

supervision of three orthopedic surgeons. We evaluated joint space measurement methods using our proposed dataset with several landmark detection approaches, including ViTPose, HRNet, PCT, YOLOv8, and U-Net. In addition, we propose using Shape Subspace (SS) for landmark refinement in heatmap-based landmark detection. The results show that the mean Euclidean distance error of joint space is 0.116 mm when using HRNet. Furthermore, the SS landmark refinement improves the mean absolute error of landmark positions by 0.010 mm with HRNet and by 0.103 mm with ViTPose on average. These highlight the potential for high-precision, real-time diagnosis of UCL injuries and associated risks, which could be leveraged in large-scale screening. Lastly, we demonstrate point-based segmentation of the humerus and ulna using the detected landmarks as input. The dataset will be made publicly available upon acceptance of this paper at: <https://github.com/Akahori000/Ultrasound-Medial-Elbow-Dataset>.

Keywords: Ultrasound Dataset, Medial Elbow, Landmark Detection, UCL injury Diagnosis, Shape Subspace

1 Background

1.1 Introduction

Ultrasound imaging is an accessible, cost-effective, and non-invasive diagnostic technique in clinical practice. In orthopedics, the screening of the medial elbows using ultrasonography is commonly performed on athletes. Some research demonstrated measuring the ulnohumeral joint space via ultrasound offers critical insights into the risk of Ulnar Collateral Ligament (UCL) injury [1, 2]. Specifically, an increased joint space under stress conditions indicates joint laxity and potential ligament damage, which can be an indicator for early diagnosis and intervention in at-risk athletes. Shanley et al. [2] measured joint space by defining landmarks on the edges of the ulna and humerus on ultrasound images. They demonstrated that pitchers with UCL injuries exhibit greater joint space than pitchers without UCL injuries (6.5 ± 1.2 mm vs 5.3 ± 1.2 mm). Michinobu et al. [3] discussed the appropriate elbow positioning during ultrasonography to effectively detect valgus laxity. However, while precise measurement is essential, the papers do not address the accuracy of the measurement method or the methods for their automation. Since ultrasound images often contain artifacts and noise, and bone shapes vary among subjects, ensuring reliable measurement is critically important.

In recent developments in deep learning, segmentation, and landmark detection have become commonly used for measuring medical ultrasound images. Segmentation has been employed to measure the thickness, circumference, and distances of anatomical parts [4–7]. Landmark detection has been applied to assess various features including distance, size, internal dimensions, and angles [8–13]. Although segmentation offers detailed shape information, its annotation is more costly than landmark detection, especially in ultrasound images where noise and artifacts blur the boundaries of

anatomical structures. Also, landmark detection can be more precise in pinpointing exact locations within anatomical structures.

Deep learning-based diagnosis using elbow ultrasound images is investigated in several studies [14–16]. These have focused on detecting osteoarthritis dissecans or identifying the median nerve in the elbows. However, no research has focused on automating the measurement of joint space. While accurate measurement of joint space in ultrasound images is essential, it is challenging due to the variability of anatomical structures and the presence of imaging artifacts. Figure 1 shows ultrasound images of the medial elbow from different subjects, and Figure 1(b) depicts enlarged views of the humerus and ulna near the joint. As shown in these figures, bone shapes vary between individuals, and the bone edges are occasionally indistinct. Moreover, confounding white lines or regions are frequently observed near the upper surfaces of the bones or in the spaces between them.

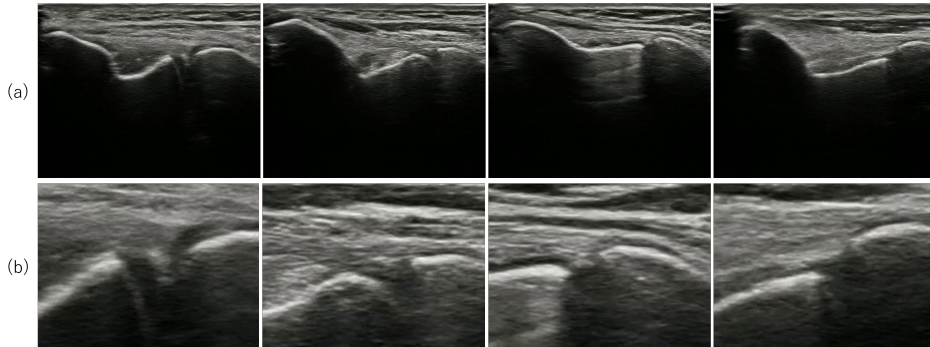


Fig. 1 (a) The ultrasound images of the medial elbow obtained from different participants (b) The enlarged views of the joint space positions. The left white line and the right white line located in the middle of each image are the humerus and ulna, respectively.

To address these challenges, a carefully annotated dataset is essential. However, no dataset currently exists for medial elbow ultrasonography aimed at measuring joint space, and developing such a medical dataset is a complex and demanding task. Data acquisition requires advanced technical skills, adherence to ethical standards, and careful respect for participants’ consent and privacy. Additionally, the quality of ultrasound images depends on the sonographer’s expertise. For medial elbow imaging, accurate probe placement on the medial epicondyle ridge is essential to capture the target structures properly. Moreover, annotation requires specialized knowledge to ensure accuracy and reliability, further complicating the development of such a dataset.

In this paper, we introduce a medial elbow ultrasound dataset comprising 4,201 images from 22 subjects with landmark annotation on the humerus and ulna under the supervision of three orthopedic surgeons. We evaluated joint space measurement methods using several landmark detection approaches with our proposed dataset. In addition, we propose using Shape Subspace (SS) for landmark refinement in heatmap-based landmark detection. The results show that the mean Euclidean distance error for joint space is 0.116mm when HRNet[17] is used, indicating that the model trained on

our dataset can automate joint space measurement with sufficient accuracy. Furthermore, the shape subspace landmark refinement improves the mean absolute error of 8 landmark positions, which suggests the effectiveness of measuring the geometric difference between point sets generated by taking the peak locations on multiple heatmaps as coordinates. These results highlight the potential for high-precision, real-time diagnosis of UCL injuries and associated risks, which could be leveraged in large-scale screening. Finally, we demonstrated point-based bone segmentation using the detected landmarks as the input, showing an application of our dataset.

1.2 Related works

1.2.1 Landmark detection

landmark Detection Methods. Landmark detection, also known as keypoint detection, is a technique used to identify specific points in images. Various methods have been proposed, particularly in the field of human pose estimation.

Regression-based approaches [18–25] directly predict landmark coordinates. While these methods are effective in simplicity and speed, they often struggle with precision in complex poses.

Heatmap-based methods overcome this by generating heatmaps where the intensity represents the likelihood of a landmark’s location, achieving better spatial accuracy. Various studies have employed Convolutional Neural Network (CNN) including [17, 26–36]. Among these, U-Net [36] and its extensions are widely used in localization tasks of medical images. The architecture utilizes skip connections to copy the feature maps from each stage of the encoder and directly pass them to the decoder’s corresponding stage, enabling precise localization using high-resolution and low-resolution information. HRNet [17] differs from earlier methods by maintaining high-resolution representations throughout the whole process, unlike an encoder-decoder network, which allows for accurate localization with multi-resolution features. Recently, Transformer-based approaches [37–40] have gained attention for their effectiveness in pose estimation task. These models leverage the self-attention mechanism to capture long-range dependencies, which enhances precision and robustness in occlusion or complex poses. TransPose [38] extracts features by CNNs, which are then processed by the transformer. ViTPose [40] has a simple architecture consisting of plain Vision Transformers as its backbone, making it computationally efficient compared to the models [38, 39].

Graph-based methods [41–44] utilize Graph Convolutional Network (GCN) to capture spatial and structural dependencies between joints, and each joint is represented as a node. These methods are often combined with heatmap-based pose estimation to either map 2D poses to 3D or enhance the inference accuracy.

Lastly, Token-based method also learns the relationships between joints by tokens. In TokenPose [45], each landmark token is designed to represent a specific joint in a body and is trained to obtain both visual features and anatomical constraint relations in Transformer layers. PCT [46] designs each token to represent a substructure of joints, where the substructure is automatically learned in the tokenizer.

Landmark Detection in Ultrasound Images. Several landmark detection approaches have been applied to ultrasound images to measure anatomical structures. For instance, U-Net and its extensions have been utilized [9, 12]. ResNet has been employed [11], and an HRNet-based pipeline [13] is proposed. Additionally, graph-based method [10] have been applied after detecting heatmaps to improve positional accuracy by modeling complex spatial relationships.

1.2.2 Geometric Representation using Shape Subspace

Shape Subspace (SS) is a method for representing the 3D points of a 3D structure as a linear subspace within a high-dimensional vector space. By measuring the similarity between two shape subspaces, the geometrical difference of 3D structures can be measured [47]. Shape subspace have been used to classify 3D objects and human faces by generating shape subspace from the 3D feature points [48, 49].

1.2.3 Point-based Segmentation

Segment Anything in Images and Videos (SAM2) [50] is designed for interactive segmentation tasks, capable of processing both images and videos. By leveraging point or bounding-box prompts, SAM2 can generate accurate segmentation masks. Its robust performance is driven by a combination of a large-scale training dataset and a transformer-based architecture, making it highly versatile for applications in medical imaging, autonomous systems, and more.

2 Method

2.1 Novel Ultrasound Elbow Dataset

2.1.1 Data Collection

We have constructed an ultrasound medial elbow dataset comprising 4,201 images from 22 participants. The participants are aged between 22 and 56, men and women, from five countries. The images are captured using a musculoskeletal ultrasonograph (SONIMAGE MX1, KONICA MINOLTA, INC., Tokyo, Japan) with an 11-MHz linear probe by two orthopedic surgeons (3 and 5 years of experience in ultrasonography of medial elbow). During the examination, the participants lay on a bed with their elbows flexed at 90 degrees following [3], and a surgeon gradually moved the gel-applied probe around the medial side as shown in Figure 2(c). The image resolution is 528×672 pixels, corresponding to 0.0567 mm per pixel. The images are flipped, as needed, to position the humerus on the left and the ulna on the right. Figure 1 shows examples of images obtained from different participants, along with the enlarged views of the joint space positions.

2.1.2 Annotation

The obtained 4,201 images were manually annotated with landmarks by the authors in consultation with the three orthopedic surgeons. The landmarks include two joint space measurement points: the distal end of humeral trochlea, and the proximal end

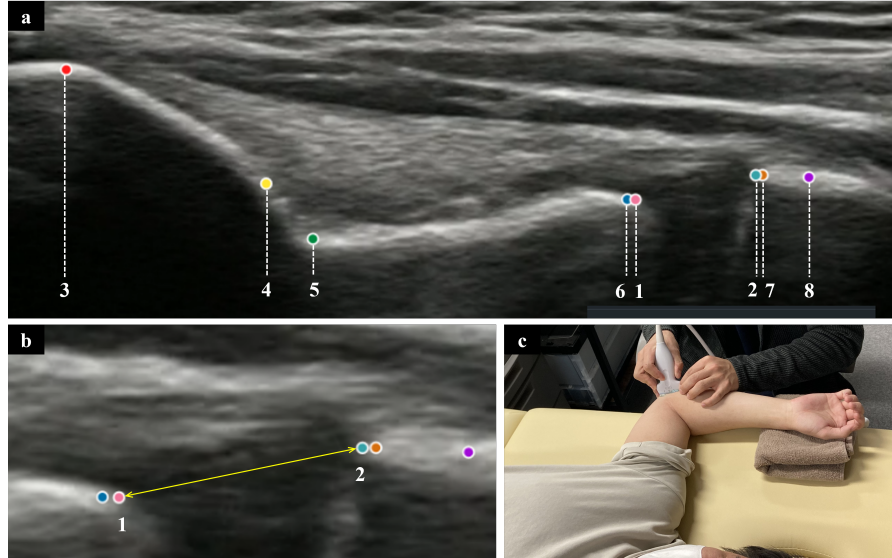


Fig. 2 (a) The annotated landmarks: 1) Distal end of humeral trochlea, 2) Proximal end of ulnar coronoid process. Landmark 1 and 2 are the joint space measurement points. 3) Tip of humeral medial epicondyle, 4) Deep end of the intersection of humeral medial epicondyle and ulnar collateral ligament, 5) Distal end of humeral medial epicondyle, 6) Proximal point adjacent to the landmark 1 on the center of hyperechoic line of humeral trochlea, 7) Distal point adjacent to the landmark 2 on the center of hyperechoic line of ulnar coronoid process, 8) Distal point of ulnar coronoid process. The white line where landmarks 1, and 3 through 6 are located is the humerus, while the line where landmarks 2, 7, and 8 are located is the ulna. (b) The enlarged view of joint space. The yellow arrow is the joint space length to be measured. Landmark 1 and 2 are the joint space measurement points. (c) The participant's posture during the examination.

of ulnar coronoid process, corresponding to the positions described in [2]. In addition to the joint space measurement points, six additional points on the humerus and ulna were annotated. These points are of particular interest to sonographers, who primarily focus on bone structures during ultrasound image interpretation. The annotations were made at sub-pixel levels for precise measurements. The landmark positions, especially those for the joint space measurement points, were meticulously reviewed and discussed by the three orthopedic experts, ensuring the reliability of the dataset.

Figure 2(a) shows the annotated landmarks. All landmarks are located on the humerus or ulna : 1) Distal end of humeral trochlea, 2) Proximal end of ulnar coronoid process. Landmark 1 and 2 are the joint space measurement points. 3) Tip of humeral medial epicondyle, 4) Deep end of the intersection of humeral medial epicondyle and ulnar collateral ligament, 5) Distal end of humeral medial epicondyle, 6) Proximal point adjacent to the landmark 1 on the center of hyperechoic line of humeral trochlea, 7) Distal point adjacent to the landmark 2 on the center of hyperechoic line of ulnar coronoid process, 8) Distal point of ulnar coronoid process. The yellow line segment between landmark 1 and 2 in Figure 2(b) shows the joint space to be measured.

2.1.3 Dataset Structure

We provide the dataset composed of ultrasound images and an annotation in a JSON file. The annotation file contains *landmark_x*, *landmark_y*, *landmark_visibility* of 8 landmarks.

2.2 Landmark Detection Models

We compare several landmark detection models: HRNet [17], ViTPose [37], and U-Net [36] as heatmap-based methods, YOLOv8 [25] as a regression-based method, and PCT [46] as a token-based method.

HRNet, ViTPose, and U-Net. The landmark detection of HRNet, ViTPose and U-Net can be represented in Equation 1, where f represents the landmark detection model, and $\mathbf{x} \in \mathbb{R}^{W \times H \times 3}$ is the input image with dimensions W (width), H (height), and 3 (channel). $f(\mathbf{x})$ is the heatmaps of size $W' \times H' \times K$, where W' and H' are the width and height of the heatmap, and K represents the number of landmarks. The $\arg \max(f(\mathbf{x}))$ operation returns the coordinates of the maximum value for each landmark heatmap, denoted as \mathbf{p}' , providing rough landmark locations. The UDP(\cdot) function, which stands for Unbiased Data Processing based on [51, 52], refines these coordinates to sub-pixel accuracy. Finally, the refined landmark positions $\mathbf{p} \in \mathbb{R}^{K \times 2}$ are calculated, where each landmark is specified by its (x, y) coordinates.

$$\mathbf{p} = \text{UDP}(\arg \max_{\mathbf{p}'}(f(\mathbf{x})), f(\mathbf{x})). \quad (1)$$

PCT and YOLOv8. Equation 2 represents the landmark detection using YOLOv8 and PCT. g is the landmark detection model. The output $g(\mathbf{x}) \in \mathbb{R}^{K \times 2}$ directly predicts the coordinates of the K landmarks.

$$\mathbf{p} = g(\mathbf{x}). \quad (2)$$

2.3 Landmark Refinement using Shape Subspace

We propose using shape subspace for landmark refinement in heatmap-based landmark detection. Heatmap-based models are trained to produce a single peak on each heatmap, however, it may occasionally generate multiple or unclear peaks. By leveraging shape subspace, the predicted landmark positions can be refined. This is achieved by selecting the most likely combinations of landmarks based on their similarity to the patterns observed in the training data.

Figure 3 provides a conceptual illustration of the shape subspace landmark refinement. A shape subspace S is computed from a shape matrix X that consists of landmark coordinates which we call point sets, and the similarity between two subspaces is computed. The key advantage of using shape subspace is its ability to represent the spatial relationships among points while remaining invariant under affine transformations applied to the point set. This means that the shape subspace remains unchanged in case of positional shifts in the entire point set or size differences of the bone structures. On the other hand, the nonlinear transformation of a point set

alters the shape subspace, making it effective for detecting differences when one or a few points among the set are shifted. As noted by Igarashi et al. [47], the order of points in the shape matrices must be consistent. Since each point is extracted from each heatmap corresponding to each landmark, this condition is always satisfied in our approach.

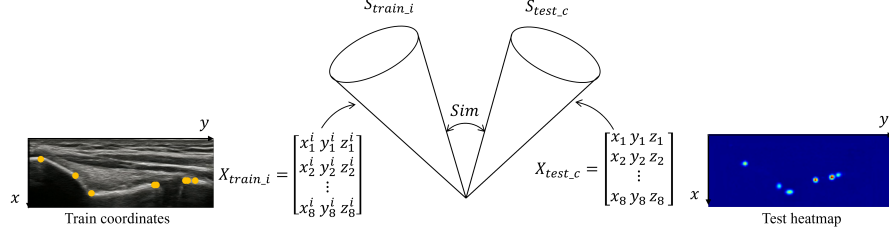


Fig. 3 The application of shape subspace to the landmark refinement. Shape matrices X_{train_i} and X_{test_c} are derived from the landmark coordinates of the training data and the test heatmaps, respectively. Shape subspace S_{train_i} and S_{test_c} are computed from the shape matrices, and the similarity between the two shape subspaces are compared. Note that, z in X_{train_i} and X_{test_c} are set to zero to generate shape subspace from 2D coordinates.

2.3.1 Shape Subspace

In this section, we provide the mathematical definition of shape subspace. Shape subspace is a method to represent a 3D point set as a 3D linear subspace within a high-dimensional vector space. As described in [47], a shape subspace S of a 3D object is calculated from a $P \times 3$ shape matrix X :

$$X = (r_1 r_2 \dots r_P)^T = \begin{pmatrix} x_1 & y_1 & z_1 \\ \vdots & \vdots & \vdots \\ x_P & y_P & z_P \end{pmatrix}, \quad (3)$$

where $r_p = (x_p \ y_p \ z_p)^T$ for $1 \leq p \leq P$ denotes the positional vector of the p th point on an object. .

Next, the shape matrix X is centered and gets X_c to satisfy the relation $\sum_{p=1}^P r_p = 0$, making the shape subspace invariant to the translation of coordinates.

$$X_c = X - \frac{1}{P} \sum_{p=1}^P r_p. \quad (4)$$

Then, compute the Singular Value Eecomposition (SVD) of the centered matrix X_c , where U , Σ , V^T are left singular vectors, singular values, and right singular vectors, respectively. The shape subspace S is defined by the first d columns of U .

$$X_c = U \Sigma V^T. \quad (5)$$

The similarity between two shape subspace $sim(S_1, S_2)$ can be measured by the canonical angles θ_i , where $\{0 \leq \theta_1, \dots, \theta_3 \leq \frac{\pi}{2}\}$.

$$\text{sim}(S_1, S_2) = \frac{1}{N} \sum_{i=1}^N \cos^2 \theta_i. \quad (6)$$

Let $\{\Phi_i\}_{i=1}^N$ be basis vectors of S_1 and $\{\Psi_i\}_{i=1}^N$ be basis vectors of S_2 . The projection matrices \mathbf{P}_1 and \mathbf{P}_2 are calculated as $\sum_{i=1}^N \Phi_i \Phi_i^T$ and $\sum_{i=1}^N \Psi_i \Psi_i^T$, respectively. $\cos^2 \theta_i$ is the i -th largest eigenvalue of $\mathbf{P}_1 \mathbf{P}_2$ or $\mathbf{P}_2 \mathbf{P}_1$.

2.3.2 The Refinement Algorithm

First, landmark coordinate candidates are obtained from heatmaps $f(\mathbf{x})$ generated by the model. From each heatmap, up to five landmark candidates are extracted. The candidates are selected in descending order based on their values of the heatmap, ensuring that each candidate is at least a distance of length threshold L away from previously selected candidates to maintain spatial separation. Also, the values of the selected candidates must exceed the value threshold $r\%$ of the maximum value of the heatmap.

Second, all possible combinations of 8 candidates are evaluated based on their similarities to the training data using shape subspace. In each combination, the similarities to M samples of the training data are calculated, and the average similarity is computed. Here, M represents a predetermined number of the total training data. Finally, the combination with the highest similarity $c^* \in \mathbb{R}^{K \times 2}$ is selected.

$$c^* = \arg \max_c \left(\frac{1}{M} \sum_{i=1}^M \text{sim}(S_{\text{train}_i}, S_{\text{test}_c}) \right). \quad (7)$$

The coordinates of the combination c^* are then input to the UDP algorithm along with the heatmaps $f(\mathbf{x})$, and the landmark positions \mathbf{p} are computed.

2.4 Point-based Bone Segmentation

As an application of landmark detection, we demonstrate the segmentation of the humerus and ulna using SAM2, with the detected landmarks as the point prompts.

2.5 Experiments

In this section, we perform landmark detection on our proposed dataset to evaluate the accuracy of joint space measurement. We assessed model performance with different landmark configurations: two-landmark detection (detecting the joint measurement points, landmark 1 and 2) and eight-landmark detection (detecting all landmarks from 1 to 8).

The dataset, consisting of 4,201 images from 22 participants, was divided by individuals into 5 groups, with 3 groups used for training, 1 group for validation, and 1 group for testing, following a 5-fold cross-validation approach. For example, 13 participants were allocated for training, 4 for validation, and 5 for testing. Considering the need to perform the inference directly on the images obtained from ultrasonography devices in clinical settings, we used full-size images without cropping for training, validation, and testing.

2.5.1 Experiment Configuration

- **The Landmark Detection Models**

ViTPose. Three input image sizes were evaluated: 256×192 pixels, 384×288 pixels, 512×384 pixels with corresponding output heatmap sizes of 64×48 pixels, 96×72 pixels, 128×96 pixels, respectively. The augmentation process included random scaling and rotation. The Normalized Mean Error (NME) was used as the evaluation metric. The total epoch was 210, with the best epoch being selected using the validation set. The optimizer was Adam. The initial learning rate was 1×10^{-4} , and it was adjusted using a step-based policy, with reductions at epochs 170 and 200. The backbone was ViT-small, and the head was the classic decoder as described in [40]. The pre-trained model trained on ImageNet [53] dataset was used. The patch size was 16×16 pixels. The joint weights of all the landmarks were set to 1.0.

HRNet. Three input image sizes 256×192 pixels, 384×288 pixels, 512×384 pixels were compared with corresponding output heatmap sizes of 64×48 pixels, 96×72 pixels, 128×96 pixels, respectively. The augmentation process included random scaling and rotation. The NME was used as the evaluation metric. The total epoch was 210, with the best epoch being selected using the validation set. The optimizer was Adam. The initial learning rate was 1×10^{-4} , and it was adjusted using a step-based policy, with reductions at epochs 170 and 200. The backbone was HRNet-w32. The pre-trained model trained on ImageNet dataset was used. The joint weights of all the landmarks were set to 1.0.

U-Net. Two input image sizes 256×256 pixels and 512×512 pixels were used, with output heatmap sizes matching the input sizes. The augmentation process included random scaling and rotation. The normalized mean error was used as the evaluation metric. The total epoch was 600, with the best epoch selected by the validation set, and the learning rate was set to 1×10^{-3} .

PCT. Two input image sizes were evaluated: 256×256 pixels. Data augmentation included random scaling, rotation, and shift. The Swin Transformer V2 backbone pre-trained with SimMIM [54] on ImageNet was used. The optimizer was AdamW, with an initial learning rate of 8×10^{-4} , which was adjusted using a cosine annealing schedule. The number of tokens was set to 34. The training epoch was set to 50 for the tokenizer and 210 for the classifier following [46]. The joint weights of all the landmarks were set to 1.0.

YOLOv8. The input image size was 640×640 pixels. The augmentation process included random rotations, scaling, shifts, and horizontal flips. Training was conducted for 1,000 epochs, with the best epoch selected for evaluation. The optimizer was AdamW for the first 10,000 iterations, followed by SGD. The initial learning rate was 1×10^{-3} for AdamW and 1×10^{-2} for SGD. The pose loss weight was set to 12.0.

- **The Number of Landmarks**

We compared two-landmark and eight-landmark detection. The two-landmark detection model detects landmarks 1 and 2. The eight-landmark model detects all

landmarks from 1 to 8. The landmark refinement is only applied to eight-landmark detection.

- **The Landmark Refinement**

The value threshold r was set to 75%, and the length threshold L was set to 5 pixels on the heatmap for the candidate selection. We used random 0.033% of the total training samples for the similarity calculation, which, for instance, corresponds to $M = 67$.

- **The Point Prompts for Point-based Segmentation**

We used the detected 6 points in the eight-landmark detection as the positive point prompts (x_i, y_i) , ($i = 3, \dots, 8$). Also, we set the 6 negative point prompts based on the detected landmark coordinates (x_4, y_3) , (x_4, y_3) , (x_5, y_4) , $(x_5, 2y_5 - y_4)$, $(x_8, 2y_5 - y_4)$, $((x_1 + x_2)/2, (y_1 + y_2)/2)$.

2.5.2 Evaluation

We used Mean Absolute Error (MAE) as a metric to evaluate the accuracy of each predicted landmark.

$$\text{MAE}_k = \frac{1}{N} \sum_{i=1}^N \sqrt{(x_{i,k} - x_{i,k}^{\text{gt}})^2 + (y_{i,k} - y_{i,k}^{\text{gt}})^2}. \quad (8)$$

where N represents the total number of test samples, $x_{j,k}$ and $y_{j,k}$ are the predicted x - and y -coordinates of the k -th landmark in the i -th image, and $x_{i,k}^{\text{gt}}$ and $y_{i,k}^{\text{gt}}$ are the ground truth coordinates of the same landmark.

Also, Euclidean Distance Error (EDE) is used to evaluate the joint space length. The EDE is defined as the mean Euclidean distance error across all N samples.

$$\text{EDE} = \frac{1}{N} \sum_{i=1}^N \left| \|\mathbf{p}_{1,i} - \mathbf{p}_{2,i}\|_2 - \|\mathbf{p}_{1,i}^{\text{gt}} - \mathbf{p}_{2,i}^{\text{gt}}\|_2 \right|.$$

where $\|\mathbf{p}_{1,i} - \mathbf{p}_{2,i}\|_2$, $\|\mathbf{p}_{2,i}^{\text{gt}} - \mathbf{p}_{2,i}^{\text{gt}}\|_2$ represent the Euclidean distances for the predicted and ground truth lengths between landmarks 1 and 2, respectively.

3 Results

This section presents the results of the two-landmark and eight-landmark detection, where the performance was evaluated using the average results of 5-fold cross-validation. The point-based bone segmentation results are also provided.

3.1 The Two-Landmark Detection

Table 1 displays the results for the two-landmark detection. LM1 and LM2 denote the MAE of landmarks 1 and 2, respectively. Ave2 indicates the average MAE of the two landmarks, while Length represents the EDE for the joint space. As shown in the table, the heatmap-based methods outperformed other approaches. Among the heatmap-based methods, HRNet with an input image size of 512×384 pixels, achieved the best performance. The average MAE for the two landmarks was 0.122, and the EDE for

Table 1 The two-landmark detection results. LM1 and LM2 represent the Mean Absolute Error (MAE) (mm) for landmarks 1 and 2, respectively. Ave2 is the average MAE of two landmarks. Length denotes the mean Euclidean distance error (mm) for joint space length. The bold values indicate the lowest error in each column. Smaller values indicate better detection performance.

Method	input size	Joint		Ave2	Length
		LM1	LM2		
ViTPose	256×192	0.195	0.233	0.214	0.249
	384×288	0.180	0.307	0.243	0.293
	512×384	0.200	0.198	0.199	0.210
HRNet	256×192	0.187	0.227	0.207	0.221
	384×288	0.149	0.137	0.143	0.140
	512×384	0.125	0.118	0.122	0.116
U-Net	256×256	0.230	0.188	0.209	0.145
	512×512	0.174	0.150	0.162	0.112
YOLOv8	640×640	1.878	2.526	2.202	1.027
PCT	256×256	0.552	0.962	0.757	0.803

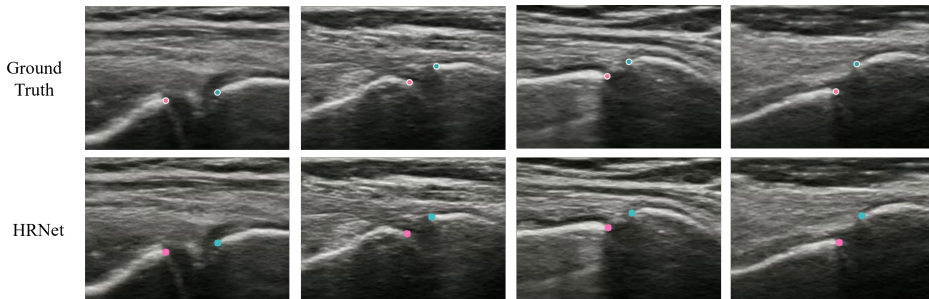


Fig. 4 The two-landmark detection results, enlarged around the joints. The upper row displays the ground truth and the lower row illustrates the inference results of HRNet with the input image size 512×384 . The pink dot is landmark1, and the light blue dot is landmark2.

the joint space was 0.112 in this configuration. Figure 4 shows the detected landmarks. As illustrated in this figure, the positions of landmarks 1 and 2 are precisely detected, even in the presence of variations in bone shapes and white noise in the joint space.

3.2 The Eight-Landmark Detection

Table 2 presents the results for the eight-landmark detection. Ave8 and Ave2 represent the average MAE for 8 landmarks (landmarks 1 - 8) and 2 landmarks (landmarks 1 and 2), respectively. Among all the conditions, HRNet + shape subspace with the input image size of 384×288 pixels achieved the best performance in the MAE across all 8 landmarks, demonstrating that shape subspace can refine landmark positions. Figure 5 illustrates the detected landmarks in the eight-landmark detection, showing that the landmarks are detected accurately. In contrast, focusing on joint measurement points (landmarks 1 and 2), the two-landmark detection using HRNet demonstrated superior performance compared to the eight-landmark detection.

Table 2 The eight-landmark detection results. LM1-LM8 represent Mean Absolute Error (mm) for landmarks 1 through 8. Ave8 is the average MAE for all 8 landmarks (LM1–LM8), and Ave2 is the average MAE for LM1 and LM2. Length denotes the mean Euclidean distance error (mm) for joint space. SS is Shape Subspace. The bold values indicate the lowest error in each column. Smaller values indicate better detection performance.

Method	input size	Joint		Humerus				Ulna		Ave8	Ave2	Length
		LM1	LM2	LM3	LM4	LM5	LM6	LM7	LM8			
ViTPose	256×192	0.210	0.251	0.424	0.463	0.682	0.213	0.245	0.468	0.369	0.231	0.260
	384×288	0.183	0.268	0.604	0.741	1.072	0.186	0.266	0.784	0.513	0.225	0.249
	512×384	0.237	0.344	1.205	1.164	2.147	0.237	0.323	1.003	0.833	0.291	0.322
ViTPose+SS	256×192	0.210	0.251	0.427	0.463	0.674	0.213	0.245	0.468	0.369	0.231	0.260
	384×288	0.183	0.259	0.566	0.608	0.798	0.186	0.258	0.594	0.432	0.221	0.245
	512×384	0.201	0.303	0.881	0.971	1.315	0.218	0.262	0.697	0.606	0.252	0.285
HRNet	256×192	0.184	0.251	0.458	0.453	0.774	0.184	0.245	0.495	0.381	0.218	0.239
	384×288	0.171	0.183	0.411	0.459	0.781	0.171	0.175	0.472	0.353	0.177	0.185
	512×384	0.148	0.154	0.495	0.529	0.976	0.152	0.147	0.471	0.384	0.151	0.158
HRNet+SS	256×192	0.184	0.251	0.458	0.453	0.774	0.184	0.245	0.495	0.381	0.218	0.239
	384×288	0.171	0.182	0.383	0.459	0.771	0.171	0.174	0.472	0.348	0.176	0.183
	512×384	0.148	0.154	0.419	0.528	0.844	0.152	0.148	0.468	0.358	0.151	0.158
U-Net	256×256	0.202	0.164	0.691	1.000	1.163	0.207	0.163	0.482	0.509	0.183	0.141
	512×512	0.175	0.173	5.556	1.666	3.326	0.180	0.148	0.698	1.490	0.174	0.150
YOLOv8	640×640	0.585	0.717	0.677	0.540	0.717	0.587	0.710	1.837	0.796	0.651	0.718
PCT	256×256	0.640	0.954	1.087	0.655	1.235	0.623	0.941	1.035	0.896	0.797	0.585

3.3 Point-based Segmentation

Figure 6 illustrates the point-based segmentation results using SAM2 with the point prompts calculated from the detected landmark positions. The green stars indicate the positive point prompts, the red stars denote the negative point prompts, and the blue areas represent the segmented regions. Compared to the ground truth, the humerus and ulna are segmented with high fidelity.

4 Discussion

First, heatmap-based methods outperformed other approaches in both the two- and eight-landmark detection. Among them, HRNet achieved the best overall performance. The ability of HRNet to capture local features while maintaining high-resolution representations makes it particularly suitable for precise landmark detection in ultrasound images. In comparison, Transformers like ViTPose tend to require larger datasets for effective training. Given the limited dataset size, HRNet’s efficiency with smaller datasets probably contributed to its superior performance.

Second, the two-landmark detection demonstrated better accuracy in joint space measurements (landmarks 1 and 2) than the eight-landmark detection model. This is likely because the simpler task of detecting fewer landmarks allows the model to focus on the most relevant features.

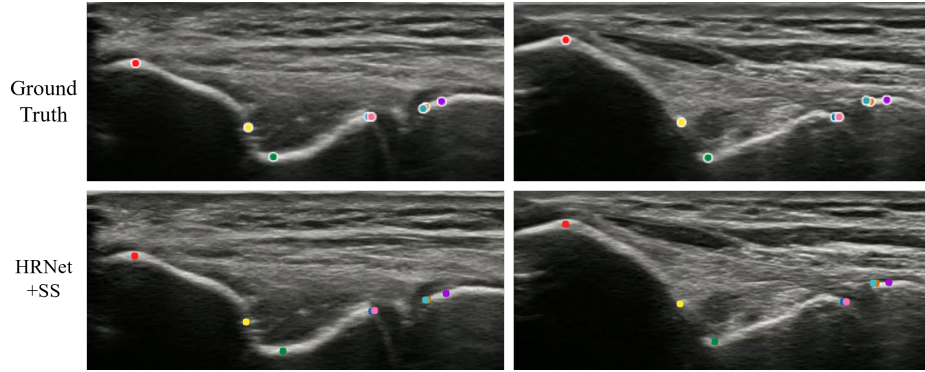


Fig. 5 The eight-landmark detection results, enlarged around the joints. The first row shows the ground truth for 8 landmarks. The second row illustrates the positions of detected landmarks by HRNet+SS with the input size 384×288 . The colors of landmarks 1 to 8 are pink, light blue, red, yellow, green, blue, orange, and purple.

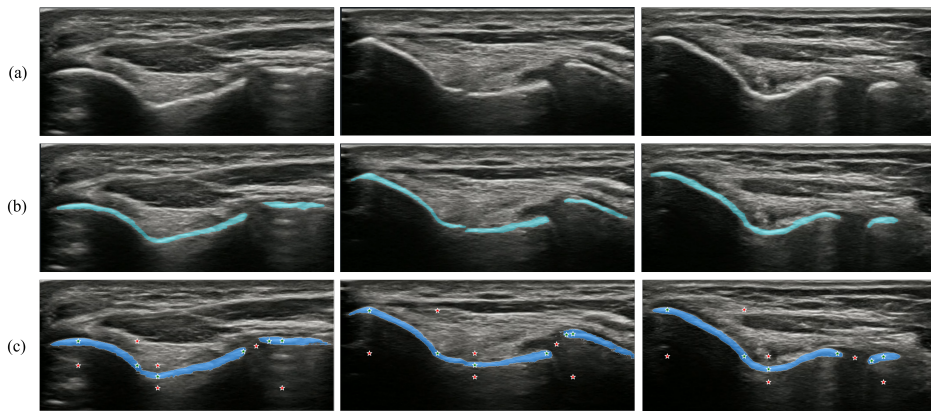


Fig. 6 The point-based segmentation results using SAM2 with the point prompts calculated by the detected landmark positions. (a) The original images, (b) The ground truth of the bone segmentation. (c) The segmented images using SAM2 and the point prompts calculated from detected landmarks. The blue areas represent the segmented regions, the green stars indicate the positive point prompts and the red stars denote the negative point prompts.

Third, in the eight-landmark detection model, the application of shape subspace was able to refine landmark positions. Figure 7 displays the refinement example. In this figure, the left images are overlays of the heatmaps and the original image, and the right image shows the refined positions of the landmarks. Among the heatmaps, the LM3 heatmap has multiple peaks, where the right peak has a higher value than the left peak. Through the shape subspace refinement, the left peak, which closely aligns with the ground truth position of landmark 3, is correctly selected, as indicated by the red point. This refinement is particularly effective in cases where multiple peaks exist in heatmaps. The performance improvement achieved through the shape subspace refinement was more pronounced in ViTPose compared to HRNet. This can

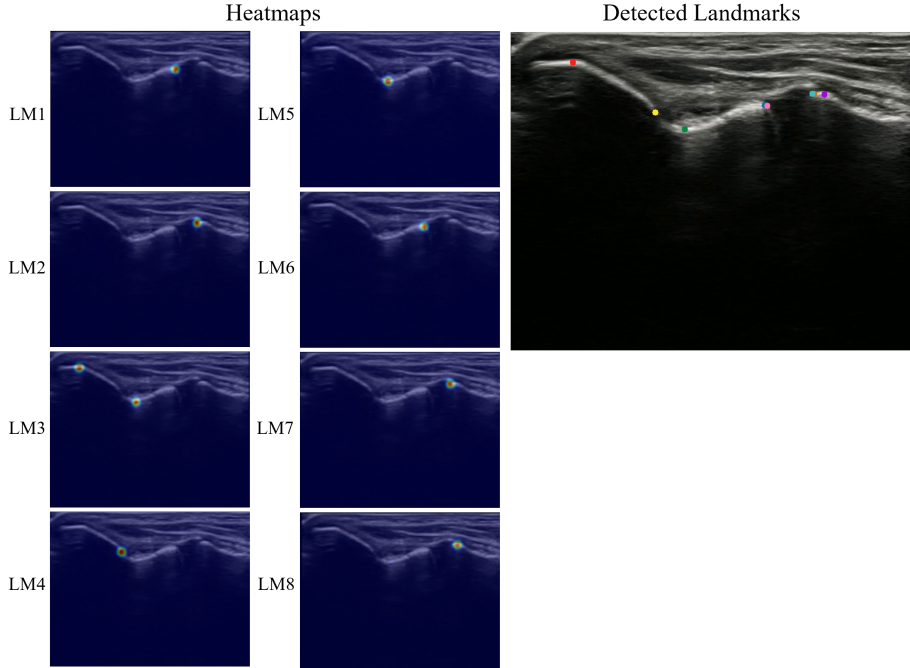


Fig. 7 An example of landmark refinement using shape subspace. The left images are overlays of the heatmaps and the original image. In LM3 heatmap, multiple peaks are present, and the left peak was selected by shape subspace, while the value was higher in the right peak. The right image shows the detected landmarks, with the red point representing the obtained position from LM3. The colors of Landmark 1 - 8 are pink, light blue, red, yellow, green, blue, orange, and purple.

be attributed to ViTPose’s ability to capture a broader context in the image, which results in multiple peaks more often in the heatmaps.

Finally, the detection accuracy achieved by our proposed method satisfies the precision required to diagnose UCL injuries using joint space measurement. While pitchers with UCL injuries exhibit average joint space increases of 1.2 mm as discussed in [2], our method achieved an average joint space measurement error of 0.116 mm when using HRNet for the two-landmark detection with an input size of 512×384 pixels.

Limitation. Here we discuss some of the known limitations of our study. To begin with, the ultrasound elbow dataset includes the ultrasound images acquired using the specific equipment, which may not fully reflect the variability in clinical settings, such as different equipment or configurations. Next, although the dataset consists of participants from diverse backgrounds, the model may have limited generalization to broader populations with different anatomical characteristics. Also, although shape subspace can refine the location of landmarks when multiple peaks are present on a heatmap, it may be challenging to refine the location when peaks are connected over a few pixels.

5 Conclusion

In this paper, we introduced a novel ultrasound dataset comprising 4,201 medial elbow images from 22 subjects for joint space measurement. The landmark annotations in this dataset were meticulously prepared under the supervision of three orthopedic experts. We evaluated joint space measurement methods and their accuracy using this dataset by applying several landmark detection models while varying the number of landmarks. The results demonstrated that HRNet achieved an EDE of 0.116 mm for joint space measurements, which is precise enough to support the diagnosis of UCL injuries. Additionally, we proposed a landmark refinement method using shape subspace, which further improved the detection performance. These results highlight the potential of our approach to allow non-invasive, real-time detection of UCL injuries and their early signs, providing valuable support for clinical decision-making. Finally, we performed point-based bone segmentation of the humerus and ulna using the detected landmark coordinates as point prompts. This showcases an application of our dataset and approach, emphasizing its versatility and clinical relevance.

6 Acknowledgement

We are grateful to Mr. Hiromitsu Tsuge for his valuable contributions to the annotation criteria for the ultrasound images used in this study. We also extend our gratitude to Dr. Akira Ikumi for the valuable medical advice. Additionally, we are grateful to Prof. Kazuhiro Fukui, Mr. Matheus Silva de Lima, and Mr. Santos Enoque Safrão for their kind advice on the shape subspace implementation. Finally, we thank Prof. Xie Chun for his insightful advice throughout this work.

References

- [1] Ciccotti, M.G., Atanda, A., Nazarian, L.N., Dodson, C.C., Holmes, L., Cohen, S.B.: Stress sonography of the ulnar collateral ligament of the elbow in professional baseball pitchers: A 10-year study. *The American Journal of Sports Medicine* **42**(3), 544–551 (2014) <https://doi.org/10.1177/0363546513516592>
- [2] Shanley, E., Smith, M., Mayer, B.K., Bailey, L.B., Thigpen, C.A., Tokish, J.M., Kissenberth, M.J., Noonan, T.J.: Using stress ultrasonography to understand the risk of ucl injury among professional baseball pitchers based on ligament morphology and dynamic abnormalities. *Orthopaedic Journal of Sports Medicine* **6**(8) (2018) <https://doi.org/10.1177/2325967118788847>
- [3] Michinobu, R., Ogawa, T., Yoshii, Y., Ikumi, A., Ikeda, K., Tsuge, H., Teruya, S., Hara, Y., Yamazaki, M.: Optimal limb position for the stress ultrasound evaluation of elbow valgus laxity in baseball players. *Orthopaedic Journal of Sports Medicine* **12**(2) (2024) <https://doi.org/10.1177/23259671231221523>
- [4] Meiburger, K.M., Marzola, F., Zahnd, G., Fajta, F., Loizou, C.P., Lainé, N., Brito Carvalho, C., Steinman, D.A., Gibello, L., Bruno, R.M., Clarenbach, R.,

- Francesconi, M., Nicolaidis, A.N., Liebgott, H., Campilho, A.J.C., Ghotbi, R., Kyriacou, E.C., Navab, N., Griffin, M., Panayiotou, A.G., Gherardini, R., Varetto, G., Bianchini, E., Pattichis, C.S., Ghiadoni, L., Rouco, J., Orkisz, M., Molinari, F.: Carotid ultrasound boundary study (cubs): Technical considerations on an open multi-center analysis of computerized measurement systems for intima-media thickness measurement on common carotid artery longitudinal b-mode ultrasound scans. *Computers in biology and medicine* **144**, 105333 (2022)
- [5] Zhu, F., Liu, M., Wang, F., Qiu, D., Li, R., Dai, C.: Automatic measurement of fetal femur length in ultrasound images: a comparison of random forest regression model and segnet. *Mathematical biosciences and engineering : MBE* **18** **6**, 7790–7805 (2021)
- [6] Kwon, H., Jung, Y.N., Jo, S.B., Lee, Y.H., Sun, S., Seo, J., Kwon, J.K.: Op08.08: Deep learning-based automated measurement of cervical length in transvaginal ultrasound images of pregnant women. *Ultrasound in Obstetrics Gynecology* (2022)
- [7] Zeng, W., Luo, J., Cheng, J., Lu, Y.: Efficient fetal ultrasound image segmentation for automatic head circumference measurement using a lightweight deep convolutional neural network. *Medical physics* (2022)
- [8] Kanauchi, Y., Hashimoto, M., Toda, N., Okamoto, S., Haque, H., Jinzaki, M., Sakakibara, Y.: Automatic detection and measurement of renal cysts in ultrasound images: A deep learning approach. *Healthcare (Basel)* **11**(4), 484 (2023) <https://doi.org/10.3390/healthcare11040484>
- [9] Gilbert, A., Holden, M., Eikvil, L., Aase, S.A., Samset, E., Mcleod, K.: Automated left ventricle dimension measurement in 2d cardiac ultrasound via an anatomically meaningful cnn approach. *ArXiv abs/1911.02448* (2019)
- [10] Feng, Y., Yang, J., Li, M., Tang, L., Sun, S., Wang, Y.: A bayesian network for simultaneous keyframe and landmark detection in ultrasonic cine. *Medical image analysis* **97**, 103228 (2024)
- [11] Hu, X., Wang, L., Yang, X., Zhou, X., Xue, W., Cao, Y., Liu, S., Huang, Y., Guo, S., Shang, N., Ni, D., Gu, N.: Joint landmark and structure learning for automatic evaluation of developmental dysplasia of the hip. *IEEE Journal of Biomedical and Health Informatics* **26**, 345–358 (2021)
- [12] Jafari, M.H., Girgis, H., Van Woudenberg, N., Liao, Z., Rohling, R., Gin, K., Abolmaesumi, P., Tsang, T.: Automatic biplane left ventricular ejection fraction estimation with mobile point-of-care ultrasound using multi-task learning and adversarial training. *International Journal of Computer Assisted Radiology and Surgery* **14**(6), 1027–1037 (2019) <https://doi.org/10.1007/s11548-019-01954-w>
- [13] Avisdris, N., Joskowicz, L., Dromey, B., David, A.L., Peebles, D., Stoyanov, D.,

- Bashat, D.B., Bano, S.: Biometrynet: Landmark-based fetal biometry estimation from standard ultrasound planes. In: International Conference on Medical Image Computing and Computer-Assisted Intervention (2022)
- [14] Inui, A., Mifune, Y., Nishimoto, H., Mukohara, S., Fukuda, S., Kato, T., Furukawa, T., Tanaka, S., Kusunose, M., Takigami, S., Ehara, Y., Kuroda, R.: Detection of elbow ocd in the ultrasound image by artificial intelligence using yolov8. *Applied Sciences* **13**(13) (2023) <https://doi.org/10.3390/app13137623>
- [15] Sasaki, K., Fujita, D., Takatsuji, K., Kotoura, Y., Minami, M., Kobayashi, Y., Sukenari, T., Kida, Y., Takahashi, K., Kobashi, S.: Deep learning-based osteochondritis dissecans detection in ultrasound images with humeral capitellum localization. *International Journal of Computer Assisted Radiology and Surgery* (2024) <https://doi.org/10.1007/s11548-023-03040-8>
- [16] Gujarati, K.R., Bathala, L., Venkatesh, V., Mathew, R.S., Yalavarthy, P.K.: Transformer-based automated segmentation of the median nerve in ultrasound videos of wrist-to-elbow region. *IEEE Transactions on Ultrasonics, Ferroelectrics, and Frequency Control* **71**(1), 56–69 (2024) <https://doi.org/10.1109/TUFFC.2023.3330539>
- [17] Wang, J., Sun, K., Cheng, T., Jiang, B., Deng, C., Zhao, Y., Liu, D., Mu, Y., Tan, M., Wang, X., Liu, W., Xiao, B.: Deep high-resolution representation learning for visual recognition. *IEEE Transactions on Pattern Analysis and Machine Intelligence* **43**(10), 3349–3364 (2021) <https://doi.org/10.1109/TPAMI.2020.2983686>
- [18] Toshev, A., Szegedy, C.: Deeppose: Human pose estimation via deep neural networks. In: Proceedings of the IEEE Conference on Computer Vision and Pattern Recognition (CVPR) (2014)
- [19] Carreira, J., Agrawal, P., Fragkiadaki, K., Malik, J.: Human pose estimation with iterative error feedback. In: 2016 IEEE Conference on Computer Vision and Pattern Recognition (CVPR), pp. 4733–4742. IEEE Computer Society, Los Alamitos, CA, USA (2016). <https://doi.org/10.1109/CVPR.2016.512> . <https://doi.ieeecomputersociety.org/10.1109/CVPR.2016.512>
- [20] Liang, S., Sun, X., Wei, Y.: Compositional human pose regression. *Computer Vision and Image Understanding* **176–177**, 1–8 (2018) <https://doi.org/10.1016/j.cviu.2018.10.006>
- [21] Zhou, X., Wang, D., Krähenbühl, P.: Objects as points. In: arXiv Preprint arXiv:1904.07850 (2019)
- [22] Geng, Z., Sun, K., Xiao, B., Zhang, Z., Wang, J.: Bottom-up human pose estimation via disentangled keypoint regression. In: 2021 IEEE/CVF Conference on Computer Vision and Pattern Recognition (CVPR), pp. 14671–14681.

- IEEE Computer Society, Los Alamitos, CA, USA (2021). <https://doi.org/10.1109/CVPR46437.2021.01444> . <https://doi.ieeecomputersociety.org/10.1109/CVPR46437.2021.01444>
- [23] Li, J., Bian, S., Zeng, A., Wang, C., Pang, B., Liu, W., Lu, C.: Human pose regression with residual log-likelihood estimation. In: ICCV (2021)
- [24] Wang, C.-Y., Bochkovskiy, A., Liao, H.-Y.M.: Yolov7: Trainable bag-of-freebies sets new state-of-the-art for real-time object detectors. In: 2023 IEEE/CVF Conference on Computer Vision and Pattern Recognition (CVPR), pp. 7464–7475 (2023). <https://doi.org/10.1109/CVPR52729.2023.00721>
- [25] Jocher, G., Chaurasia, A., Qiu, J.: YOLOv8 (2023). <https://github.com/ultralytics/ultralytics>
- [26] Tompson, J., Jain, A., LeCun, Y., Bregler, C.: Joint training of a convolutional network and a graphical model for human pose estimation. In: Proceedings of the 27th International Conference on Neural Information Processing Systems - Volume 1, pp. 1799–1807. MIT Press, Cambridge, MA, USA (2014)
- [27] Wei, S., Ramakrishna, V., Kanade, T., Sheikh, Y.: Convolutional pose machines. In: 2016 IEEE Conference on Computer Vision and Pattern Recognition (CVPR), pp. 4724–4732. IEEE Computer Society, Los Alamitos, CA, USA (2016). <https://doi.org/10.1109/CVPR.2016.511>
- [28] Newell, A., Yang, K., Deng, J.: Stacked hourglass networks for human pose estimation. In: Leibe, B., Matas, J., Sebe, N., Welling, M. (eds.) Computer Vision – ECCV 2016, pp. 483–499. Springer, Cham (2016)
- [29] Bulat, A., Tzimiropoulos, G.: Human pose estimation via convolutional part heatmap regression. In: Leibe, B., Matas, J., Sebe, N., Welling, M. (eds.) Computer Vision – ECCV 2016, pp. 717–732. Springer, Cham (2016)
- [30] Newell, A., Huang, Z., Deng, J.: Associative embedding: end-to-end learning for joint detection and grouping. In: Proceedings of the 31st International Conference on Neural Information Processing Systems. NIPS’17, pp. 2274–2284. Curran Associates Inc., Red Hook, NY, USA (2017)
- [31] Yang, W., Li, S., Ouyang, W., Li, H., Wang, X.: Learning feature pyramids for human pose estimation. In: 2017 IEEE International Conference on Computer Vision (ICCV), pp. 1290–1299 (2017). <https://doi.org/10.1109/ICCV.2017.144>
- [32] Cao, Z., Hidalgo, G., Simon, T., Wei, S., Sheikh, Y.: Openpose: Realtime multi-person 2d pose estimation using part affinity fields. *IEEE Transactions on Pattern Analysis and Machine Intelligence* **43**(01), 172–186 (2021) <https://doi.org/10.1109/TPAMI.2019.2929257>

- [33] Chen, Y., Wang, Z., Peng, Y., Zhang, Z., Yu, G., Sun, J.: Cascaded pyramid network for multi-person pose estimation. In: Proceedings of the IEEE Conference on Computer Vision and Pattern Recognition (CVPR) (2018)
- [34] Cheng, B., Xiao, B., Wang, J., Shi, H., Huang, T.S., Zhang, L.: Higherhrnet: Scale-aware representation learning for bottom-up human pose estimation. In: 2020 IEEE/CVF Conference on Computer Vision and Pattern Recognition (CVPR), vol. 1, pp. 5385–5394 (2020). <https://doi.org/10.1109/CVPR42600.2020.00543>
- [35] Zhang, F., Zhu, X., Dai, H., Ye, M., Zhu, C.: Distribution-aware coordinate representation for human pose estimation. In: 2020 IEEE/CVF Conference on Computer Vision and Pattern Recognition (CVPR), pp. 7091–7100 (2020)
- [36] Ronneberger, O., Fischer, P., Brox, T.: U-net: Convolutional networks for biomedical image segmentation. In: Navab, N., Hornegger, J., Wells, W.M., Frangi, A.F. (eds.) Medical Image Computing and Computer-Assisted Intervention – MICCAI 2015, pp. 234–241. Springer, Cham (2015)
- [37] Su, K., Yu, D., Xu, Z., Geng, X., Wang, C.: Multi-person pose estimation with enhanced channel-wise and spatial information. In: 2019 IEEE/CVF Conference on Computer Vision and Pattern Recognition (CVPR), pp. 5667–5675 (2019). <https://doi.org/10.1109/CVPR.2019.00582>
- [38] Yang, S., Quan, Z., Nie, M., Yang, W.: Transpose: Keypoint localization via transformer. In: 2021 IEEE/CVF International Conference on Computer Vision (ICCV), pp. 11782–11792 (2021). <https://doi.org/10.1109/ICCV48922.2021.01159>
- [39] Yuan, Y., Fu, R., Huang, L., Lin, W., Zhang, C., Chen, X., Wang, J.: Hrformer: High-resolution vision transformer for dense predict. In: Ranzato, M., Beygelzimer, A., Dauphin, Y., Liang, P.S., Vaughan, J.W. (eds.) Advances in Neural Information Processing Systems, vol. 34, pp. 7281–7293 (2021)
- [40] Xu, Y., Zhang, J., Zhang, Q., Tao, D.: Vitpose: simple vision transformer baselines for human pose estimation. In: Proceedings of the 36th International Conference on Neural Information Processing Systems. NIPS '22. Curran Associates Inc., Red Hook, NY, USA (2024)
- [41] Cai, Y., Ge, L., Liu, J., Cai, J., Cham, T.-J., Yuan, J., Thalmann, N.M.: Exploiting spatial-temporal relationships for 3d pose estimation via graph convolutional networks. In: 2019 IEEE/CVF International Conference on Computer Vision (ICCV), pp. 2272–2281 (2019). <https://doi.org/10.1109/ICCV.2019.00236>
- [42] Ci, H., Wang, C., Ma, X., Wang, Y.: Optimizing network structure for 3d human pose estimation. In: 2019 IEEE/CVF International Conference on Computer Vision (ICCV), pp. 2262–2271 (2019). <https://doi.org/10.1109/ICCV.2019.00235>

- [43] Wang, J., Long, X., Gao, Y., Ding, E., Wen, S.: Graph-pcnn: Two stage human pose estimation with graph pose refinement. In: *Computer Vision – ECCV 2020*, pp. 492–508. Springer, Cham (2020)
- [44] Zhao, L., Peng, X., Tian, Y., Kapadia, M., Metaxas, D.N.: Semantic graph convolutional networks for 3d human pose regression. In: *2019 IEEE/CVF Conference on Computer Vision and Pattern Recognition (CVPR)*, pp. 3420–3430 (2019). <https://doi.org/10.1109/CVPR.2019.00354>
- [45] Li, W., Wang, Z., Yang, S., Liu, Y., Yang, W., Xu, X., Gao, Y.: Tokenpose: Learning keypoint tokens for human pose estimation. *arXiv preprint arXiv:2104.03516* **2021**, 1293–1301 (2021) <https://doi.org/10.1109/ICCV48922.2021.00129>
- [46] Geng, Z., Wang, C., Wei, Y., Liu, Z., Li, H., Hu, H.: Human pose as compositional tokens. In: *Proceedings of the IEEE/CVF Conference on Computer Vision and Pattern Recognition (CVPR)*, pp. 660–671 (2023)
- [47] Igarashi, Y., Fukui, K.: 3d object recognition based on canonical angles between shape subspaces. In: Kimmel, R., Klette, R., Sugimoto, A. (eds.) *Computer Vision – ACCV 2010*, pp. 580–591. Springer, Berlin, Heidelberg (2011)
- [48] Yoshinuma, T., Hino, H., Fukui, K.: Personal authentication based on 3d configuration of micro-feature points on facial surface. In: Bräunl, T., McCane, B., Rivera, M., Yu, X. (eds.) *Image and Video Technology*, pp. 433–446. Springer, Cham (2016)
- [49] Yataka, R., Fukui, K.: Three-dimensional object recognition via subspace representation on a grassmann manifold. In: *International Conference on Pattern Recognition Applications and Methods* (2017)
- [50] Ravi, N., Gabeur, V., Hu, Y.-T., Hu, R., Ryali, C., Ma, T., Khedr, H., Rädle, R., Rolland, C., Gustafson, L., Mintun, E., Pan, J., Alwala, K.V., Carion, N., Wu, C.-Y., Girshick, R., Dollár, P., Feichtenhofer, C.: Sam 2: Segment anything in images and videos. *arXiv preprint arXiv:2408.00714* (2024)
- [51] Huang, J., Zhu, Z., Guo, F., Huang, G.: The devil is in the details: Delving into unbiased data processing for human pose estimation. In: *Proceedings of the IEEE/CVF Conference on Computer Vision and Pattern Recognition (CVPR)* (2020)
- [52] Zhang, F., Zhu, X., Dai, H., Ye, M., Zhu, C.: Distribution-aware coordinate representation for human pose estimation. In: *Proceedings of the IEEE/CVF Conference on Computer Vision and Pattern Recognition (CVPR)* (2020)
- [53] Deng, J., Dong, W., Socher, R., Li, L.-J., Li, K., Fei-Fei, L.: Imagenet: A large-scale hierarchical image database. In: *2009 IEEE Conference on Computer Vision and Pattern Recognition*, pp. 248–255 (2009). <https://doi.org/10.1109/CVPR>.

2009.5206848

- [54] Xie, Z., Zhang, Z., Cao, Y., Lin, Y., Bao, J., Yao, Z., Dai, Q., Hu, H.: Simmim: a simple framework for masked image modeling. In: 2022 IEEE/CVF Conference on Computer Vision and Pattern Recognition (CVPR), pp. 9643–9653 (2022). <https://doi.org/10.1109/CVPR52688.2022.00943>